Storm Time Electrified MSTIDs Observed over Mid-Latitude North America

I. J. Kelley [1], B. S. R. Kunduri[1], J. B. H. Baker [1], J. M. Ruohoniemi [1], S. G. Shepherd [2]

[1]Bradley Department of Electrical and Computer Engineering, Virginia Tech, Blacksburg, Virginia, USA.
[2]Thayer School of Engineering, Dartmouth College, Hanover, NH, USA

Key Points:

- MSTID signatures were observed in GNSS TEC and SuperDARN ionospheric backscatter during a strong geomagnetic storm.
- MSTID characteristics were broadly consistent between the datasets, with periods of 10-20 min and phase speeds of ∼800 m/s.
- SuperDARN LOS velocities systematically switched polarities between MSTID crests and troughs, indicating polarization electric fields.

Corresponding author: I. J. Kelley, ikelley@vt.edu

Abstract

Medium-scale Traveling Ionospheric Disturbances (MSTIDs) are prominent and ubiquitous features of the mid-latitude ionosphere, and are observed in Super Dual Auroral Radar Network (SuperDARN) and high-resolution Global Navigational Satellite Service (GNSS) Total Electron Content (TEC) data. The mechanisms driving these MSTIDs are an open area of research, especially during geomagnetic storms. Previous studies have demonstrated that night-side MSTIDs are associated with an electrodynamic instability mechanism like Perkins, especially during geomagnetically quiet conditions. However, day-side MSTIDs are often associated with atmospheric gravity waves. Very few studies have analyzed the mechanisms driving MSTIDs during strong geomagnetic storms at mid-latitudes. In this study, we present mid-latitude MSTIDs observed in de-trended GNSS TEC data and SuperDARN radars over the North American sector, during a geomagnetic storm (peak Kp reaching 9) on September 7-8, 2017. In SuperDARN, MSTIDs were observed in ionospheric backscatter with Line Of Sight (LOS) velocities exceeding 800 m/s. Additionally, radar LOS velocities oscillated with amplitudes reaching $\pm$500 m/s as the MSTIDs passed through the fields-of-view. In detrended TEC, these MSTIDs produced perturbations reaching $\sim$50 percent of background TEC magnitude. The MSTIDs were observed to propagate in the westward/south-westward direction with a time period of $\sim$15 minutes. Projecting de-trended GNSS TEC data along SuperDARN beams showed that enhancements in TEC were correlated with enhancements in SuperDARN SNR and positive LOS velocities. Finally, SuperDARN LOS velocities systematically switched polarities between the crests and the troughs of the MSTIDs, indicating the presence of polarization electric fields and an electrodynamic instability process during these MSTIDs.

1 Introduction

Traveling Ionospheric Disturbances (TIDs) (Munro, 1948) are wave-like structures which propagate through the ionosphere. TIDs are most commonly expected to be driven by Atmospheric Gravity Waves (AGWs) originating in the neutral atmosphere (Hines, 1960) and can be sensed with instruments used for monitoring ionospheric dynamics such as Global Navigational Satellite Service (GNSS) Total Electron Content (TEC) (Saito et al., 1998) and coherent scatter radars (Samson et al., 1990; Fukao et al., 1991). TIDs are further classified as either Large-Scale (LSTIDs) or MSTIDs based on their spatio-temporal scales (Georges, 1968). MSTIDs typically have a time-period of 15-60 minutes, phase velocities of 100-300 m/s, and wavelengths between 200-800km. On the other hand LSTIDs have phase speeds between 400-1000 m/s, periods above 30 minutes, and wavelengths above 1000 km (Hocke & Schlegel, 1996; Hunsucker, 1982). The differences between MSTIDs and LSTIDs are not just limited to their spatio-temporal scales, previous studies have shown that the underlying generation mechanisms and the physics of their propagation also differ (Hocke & Schlegel, 1996). MSTIDs are often linked to Atmospheric Gravity Waves (AGWs), which are a neutral atmospheric phenomenon generally carrying more energy than the TIDs themselves (Hunsucker, 1982). Such AGW-driven MSTIDs are more commonly reported at high latitudes, and on the day-side, and in the winter (Bristow et al., 1994; Frissell et al., 2014). The AGWs are in turn expected to be driven by factors such tropospheric weather (Chou et al., 2017), Joule heating (Chimonas & Hines, 1970), and ground-based disturbances including tsunamis and earthquakes (Liu et al., 2011). Determining the sources of AGWs/MSTIDs can be challenging since they travel thousands of kilometers from the source and dissipate along the propagation paths (e.g., Vadas, 2007; Ogawa et al., 2009). Previous studies have demonstrated the utility of SuperDARN for analyzing MSTIDs (e.g., Samson et al., 1990; Bristow et al., 1994; Grocott et al., 2013; Frissell et al., 2014). In particular, these studies have shown that quasiperiodic density rarefactions and enhancements in ionospheric layers produced by MSTIDs manifest as moving bands of enhanced ground scatter power in SuperDARN observations.

In addition to AGWs, MSTIDs have also been associated with electrodynamic instabilities (Perkins, 1973; Miller, 1997). Such MSTIDs are linked to perturbations and oscillations in electric fields (e.g., Shiokawa et al., 2003; Otsuka et al., 2004, 2007; Suzuki et al., 2009). A few studies showed that these electrodynamic instabilities can map into the other hemisphere along magnetic field lines and drive MSTIDs in the conjugate location (Otsuka et al., 2004; Valladares & Sheehan, 2016). Electrified MSTIDs exhibit properities that are different from those linked to AGWs. Specifically, electrified MSTIDs were frequently observed on the night-side, propagating southwestwards. A majority of previous studies have reported electrified MSTIDs during quiet geomagnetic conditions and in summer months (Ogawa et al., 2009; Duly et al., 2013; Huang et al., 2016). Electrified MSTIDs are an active area of research and the mechanisms seeding the instability processes are yet to be fully understood. For example, it has been shown that the growth rate of the instability alone is not sufficient to seed nighttime MSTIDs (Garcia et al., 2000), and coupling with the E-region and sporadic-E instabilities can re-inforce the process (Otsuka et al., 2007; Ogawa et al., 2009). A few previous studies have used measurements from airglow imagers or TEC in combination with SuperDARN observations of electric fields to analyze the behavior and characteristics of electrified MSTIDs during geomagnetically quiet conditions (e.g., Ogawa et al., 2009; Suzuki et al., 2009). Two main features were reported by these studies. First, the Doppler Line of Sight (LOS) velocities switched polarities as the crests and troughs associated with the MSTIDs passed through the radar's field-of-view. Secondly, depletions in airglow intensity and TEC were correlated with enhancements in SuperDARN ionospheric backscatter power.

Geomagnetic storms have often been shown to drive significant LSTID activity (e.g. Ding et al., 2007; Borries et al., 2009). However, very few studies have reported and analyzed storm-time MSTIDs (e.g., S. R. Zhang et al., 2019). Such disturbed intervals can be challenging to analyze since several different factors such as neutral winds, Sub-Auroral Polarization Streams (SAPS), and strong ion-neutral coupling can be active simultaneously (Guo et al., 2018; S. R. Zhang et al., 2019), especially at mid-latitudes. For example, Guo et al. (2018) suggested that thermospheric heating by SAPS electric fields can induce regional disturbances which manifest as AGWs and TIDs. In addition, changes in neutral winds induced by SAPS electric fields (e.g., S. Zhang et al., 2017) can drive changes in the propagation of AGWs and associated TIDs. While Joule heating during geomagnetic storms is expected to drive AGWs and TIDs, a few studies have hypothesized the possibility that electrodynamic instabilities can also play a role (S. R. Zhang et al., 2019). Overall, there has been very limited focus on analyzing the role of electrodynamic instabilities in driving MSTIDs during geomagnetic storms.

In this study, US mid-latitude SuperDARN observations are used alongside high-resolution GNSS TEC data to analyze MSTID activity during a strong geomagnetic storm that took place on Sep 7-8, 2017. The MSTID characteristics (wavelength, time period, etc) are derived from these two datasets are compared. We determine that the MSTID activity in this event was associated with an electrodynamic instability.

2 Datasets

The Fort Hays, Kansas, and Christmas Valley, Oregon, mid-latitude SuperDARN radars are used to study the MSTIDs observed during this event. High-resolution GNSS TEC in the North American sector is used in conjunction with SuperDARN to characterize the MSTIDs. In this section, these datasets will be defined. Their coverage, techniques, and data will be outlined in the following section. Additionally, datasets used for capturing geomagnetic indices will be defined.

2.1 SuperDARN

SuperDARN is a global network of High-Frequency (HF) radars covering polar, high, and mid-latitudes in the Northern and Southern Hemispheres (Greenwald et al., 1995; Chisham et al., 2007; Nishitani et al., 2019). SuperDARN radars observe coherent backscatter from decameter-scale irregularities aligned along the geomagnetic field. The Doppler velocity of the back-scattered signal is proportional to the LOS component of E $\times$ B plasma drift within the scattering region (Ruohoniemi et al., 1987). The radars electronically steer across different look directions. A radar typically scans through 16 beams in 1 minute, covering $\sim$50° of azimuth. The first SuperDARN radar came into operation at Goose Bay, Labrador (Canada) in 1983. Over the following decades many others were built to improve coverage across the high-latitude regions of both the Northern and Southern Hemispheres. The SuperDARN network later expanded to the mid-latitudes to enable observations of plasma convection during intervals of very strong geomagnetic activity when the auroral oval and convection extend equatorwards (Baker et al., 2007; Nishitani et al., 2019). The most commonly used SuperDARN parameters include power which is measured in dB of SNR above the noise floor, and LOS Doppler velocities.

2.2 GNSS Total Electron Content

Total Electron Content (TEC) is a columnar electron density measurement between a satellite and ground-based receiver. Using Global Navigational Satellite Service (GNSS) constellations allows for widespread TEC measurements across the globe. TEC is typically measured in TEC units (TECu), where 1 TECu=$10^{16}\, electrons/m^2$. Worldwide GNSS TEC data is collected and processed at the MIT Haystack Observatory and available from the Madrigal database (http://www.openmadrigal.org) (Rideout & Coster, 2006; Vierinen et al., 2016). Several previous studies have shown the utility of GNSS TEC data for monitoring and analyzing MSTIDs over large geographical regions (e.g., Tsugawa et al., 2007; S. R. Zhang et al., 2017, 2019). Data is available at 30 second time cadence, which is more than sufficient for observing MSTID activity (Saito et al., 1998). Each LOS GNSS TEC data point contains satellite, receiver, latitude, longitude, elevation angle, and timestamp, along with the TEC value. Both the American GPS constellation and Russian GLONASS constellation are sources of data in this study. All data points with low elevation angles ($< 30°$ between ray-path and horizon) have been discarded to increase confidence in the measurements. Additionally, vertical TEC values were derived by accounting for the elevation angles. The TEC data from each satellite-receiver pair is de-trended by subtracting a rolling average over a 30-minute sliding window. This approach is similar to the methods discussed in S. R. Zhang et al. (2017) and Lyons et al. (2019), and preferentially selects TIDs with periods less than 30 minutes. High frequency components/noise were not filtered out in this approach. MSTIDs during this event were large in amplitude and prominent, so TEC data processing is not as consequential as compared to geomagnetically quiet intervals when perturbations in TEC are smaller.

2.3 Solar wind, IMF and geomagnetic indices

In the current study, 1-min averaged OMNI values (King & Papitashvili, 2005), time shifted to the bow shock sub-solar point were used to examine the Interplanetary Magnetic Field (IMF) and solar wind conditions. The impact of geomagnetic disturbances on mid-latitudes electrodynamics were examined using the asymmetric (Asym-H) and symmetric (Sym-H) disturbance indices (Iyemori, 1990). Note that the Sym-H and Asym-H indices have a temporal resolution of 1-minute. Finally, the impact of auroral electrojets during the event was analyzed using the AL and AU indices (Davis & Sugiura, 1966).

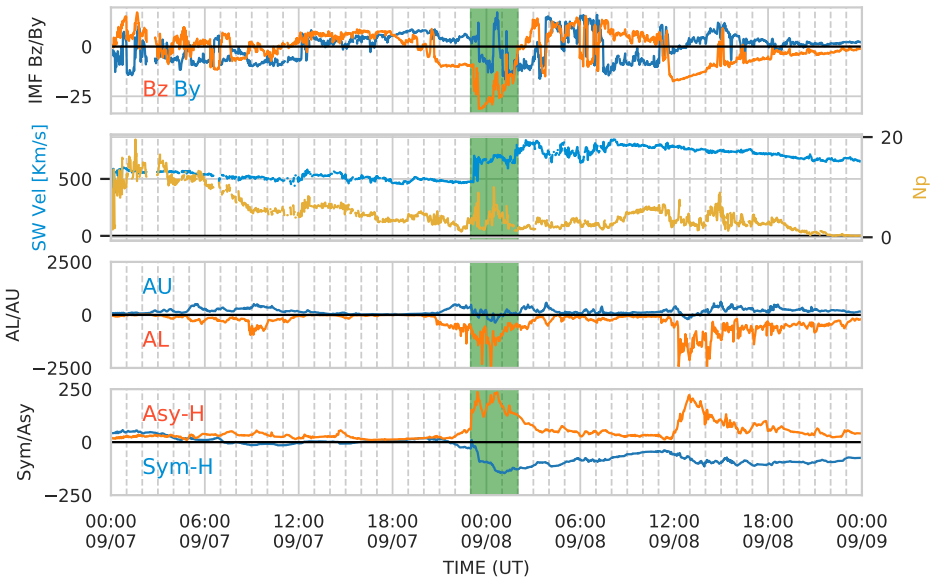

Figure 1. An overview of the geomagnetic conditions on September 7th and 8th, 2017. The conditions are shown over a 48 hour window, with the relevant time period for this study highlighted in green. The top two panels show IMF Bz/By, solar wind speed and density from the OMNI dataset. Third panel shows the auroral electrojet indices AU and AL, and the fourth panel shows the Sym-H/Asy-H indices.

3 Results

3.1 Event Overview

The event analyzed in this study occurred during the main phase of a major geomagnetic storm on Sep 7-8, 2017. Kp reached a peak of 9 at ∼1:30 UT on September 8th, 2017. An overview of the geomagnetic conditions over a 48-hour interval is presented in Figure 1. From top to bottom, the figure presents IMF Bz and By components, solar wind velocty (Vx) and number density, AL and AU indices, and Sym-H and Asy-H indices. The specific period of interest for this study is highlighted in the figure as the time interval between 23 UT on Sep 7, 2017 and 2 UT on Sep 8, 2017. It can be noted that IMF Bz turns sharply negative at ∼23:00 UT on the 7th, dropping to ∼-30 nT by 0:00 UT on the 8th. Around the same time, solar wind velocity increases from km/s to 700 km/s along with multiple upturns in number density. We note that the Sym-H index drops to ∼-200 nT during the interval of interest, marking the main phase of the geomagnetic storm. Finally, elevated AL magnitude (∼-2500 nT) and upticks in the Asy-H index (reaching 250 nT) are indicative of strong substorm activity and enhancement of the partial ring current. Overall, MSTIDs analyzed in this study occurred during an interval of strong geomagnetic driving when SAPS is expected to dominate the sub-auroral ionosphere with velocities reaching several hundred m/s (Kunduri et al., 2018; S. R. Zhang et al., 2019).

3.2 GNSS TEC Observations

A snapshot of raw and de-trended GNSS TEC measurements during the main phase of the storm at 0 UT on Sep 8, 2017 is presented in Figure 2. The top panel of the figure shows raw TEC measurements over the North American continent and the bottom

panel show the 30-minute de-trended TEC, scaled according to the color bar on the right. The outlines of Christmas Valley East beam 18, Fort Hays West beam 18, and Fort Hays East beam 14 are overlaid in the top-panel to provide context when comparing TEC measurements with SuperDARN in later sections. The de-trended TEC data shows a complex TID pattern including both LSTIDs and MSTIDs. The focus of this study is the MSTID activity observed in the north-central United States, centered around 45°N, 95°W (see region outlined in Figure 2.b). For reference, this location is about 150km west of Minneapolis, Minnesota. An important feature is that the MSTIDs are collocated with a trough-like feature observed in raw TEC data. A previous study (S. R. Zhang et al., 2019) reported observations of SAPS by the Millstone Hill ISR during the event, suggesting these MSTIDs could be linked to SAPS flows. The MSTID phase fronts are oriented North-Northwest to South-Southeast, suggesting that the direction of propagation is West-Southwest.

The propagation direction is shown in Figure 3 which displays de-trended TEC as a function of latitude vs UT (top panel) and longitude vs UT (bottom panel). This figure considers the de-trended TEC sampled geographically within the region of between 43-47°N and 108-112°W. As the sampled region is small relative to the MSTID structures, the latitude and longitude plots appear similar. The sampled region for Figure 3 is in the Western portion of the the red highlighted area in Figure 2. The perturbations in de-trended TEC are particularly strong, reaching an amplitude of ±4 TECu which forms a significant proportion of the background TEC, which varies between 10-20 TECu. In Figure 3.a, a slight equator-wards component can be detected. The Westwards velocity component (∼1 degree per minute) is stronger than the Southward component. The period of the MSTIDs are consistent between both plots. This period varies from ∼7-20 minutes throughout the interval from 0 UT to 2 UT. In the next sections, the perturbations in de-trended TEC will be compared with SuperDARN observations and the role of different factors such as electric fields in driving these MSTIDs will be analyzed.

3.3 SuperDARN Observations

The US mid-latitude SuperDARN radars were making measurements over the North American sector during the event. Of particular interest are the Christmas Valley East (CVE), Christmas Valley West (CVW), Fort Hays East (FHE), and Fort Hays West (FHW) radars. Fields-of-view of these radars cover the region where MSTIDs were observed in GNSS TEC. A snapshot of the measurements from the FHE and FHW radars at 0 UT on Sep 8, 2017 (same time presented in Figure 2) is shown in Figure 4. The top panel shows the LOS velocities observed by the radars and the bottom panel shows the power, scaled according to the color bar on the right. The red outline in the bottom panel marks the same region outlined in Figure 2 where MSTID activity was observed. We can note that SuperDARN backscatter power exhibits zonal variability, alternating between high and low-powered regions. It can also be noted that the radars were observing ionospheric backscatter with LOS speeds reaching 1 km/s. Another feature that stands out is the systematic transition from positive LOS velocities (blue colored) in FHE to negative LOS velocities (red colored) in FHW. This behavior suggests that the background plasma convection in the region is predominantly westwards. Multiple US mid-latitude SuperDARN radars observed strong ionospheric backscatter with LOS speeds reaching 1 km/s in the region where MSTIDs were observed in GNSS TEC data.

3.4 Comparison Between SuperDARN and GNSS TEC Observations

Projecting high-resolution GNSS TEC data along SuperDARN beams allows for direct comparison of the spatio-temporal variability observed in both datasets. GNSS TEC data is assumed to be sourced from a single pierce-point, which can be mapped within a given radar beam's footprint, with associated slant range and time. Note that the slant range for GNSS TEC is not limited to 45km bins as would be the case for SuperDARN

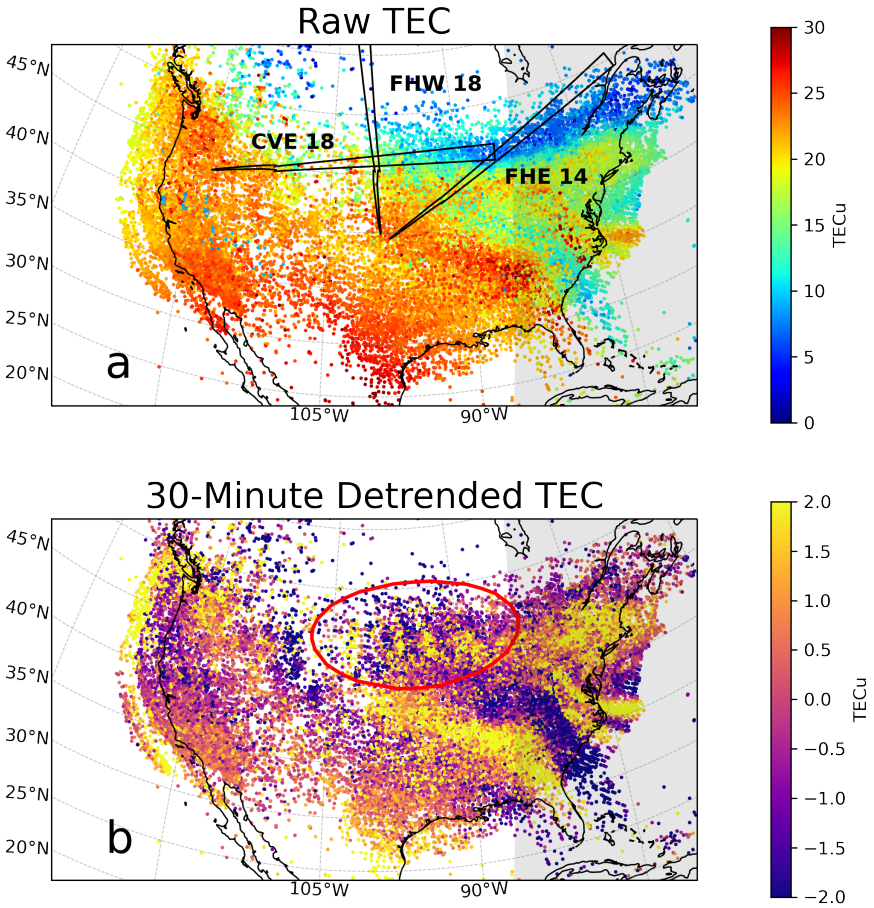

Figure 2. GNSS TEC observations over the North American sector on Sep 8, 2017 at 0:00 UT. Panel (a) shows raw TEC measurements. The outlines of Christmas Valley East radar beam 18, Fort Hays West radar beam 18, and Fort Hays East radar beam 14 are also overlaid on the map. Panel (b) shows 30-minute detrended TEC and the red outline indicates the region of interest with clear MSTID signatures. The grey shaded region denotes the day-night terminator.

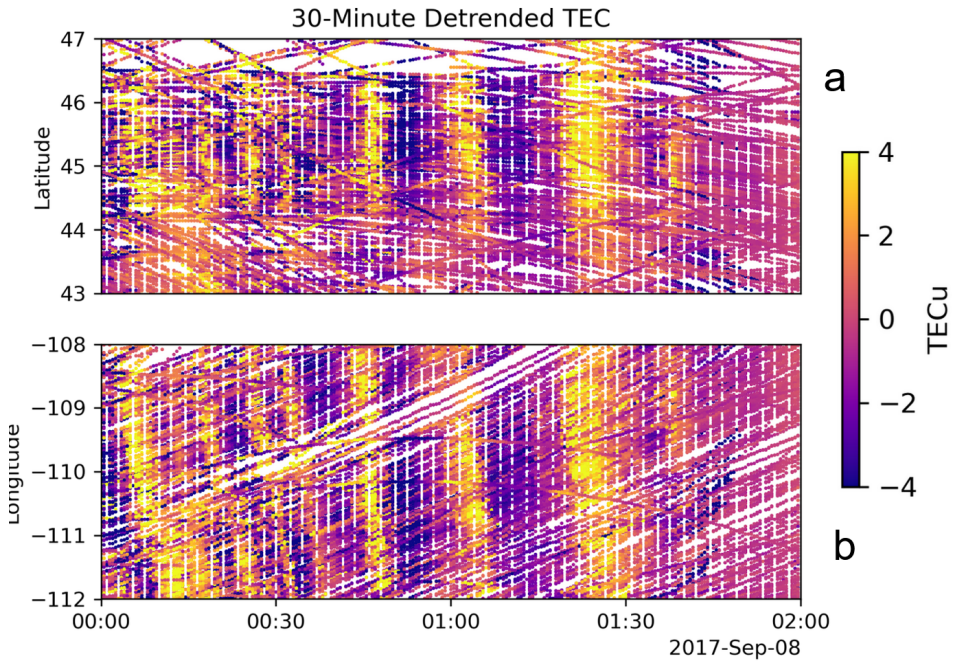

Figure 3. Spatio-temporal variability from TEC sampled with a limited 4x4 degree area. (a) shows de-trended TEC plotted as a function of latitude and UT plot and (b) shows de-trended TEC as a function of longitude and UT. TEC data for this plot is taken between 43-47°N and 108-112°W which corresponds to approximately 800km in slant range on Christmas Valley East beam 18.

data, and instead can be considered a continuous measurement. Similarly, the high-resolution GNSS TEC data has a 30 second time cadence, which is twice as fast as SuperDARN data which takes 1-2 minutes to complete a full scan across all beams. Despite the differences in the spatial and temporal resolutions of these datasets, this technique enables a direct comparison between observations made by a specific radar beam and the GNSS TEC within that beam. Figure 5 demonstrates a comparison along beam 18 of the CVE radar (left most beam marked Figure 2.a). Panel (a) of the figure presents de-trended TEC data projected along the beam, panel (b) presents the backscatter power observed on the beam, and panel (c) shows both the overlaid on top of each other. Similar to the observations presented in Figure 2 strong perturbations can be clearly noted from panel (a) starting ∼2330 UT on Sep 7 and continuing until 2 UT on Sep 8. A very similar "striation" in SuperDARN power can be observed in panel (b) with enhancements in backscatter power reaching 40 dB. Another interesting feature is that the "striations" can be observed at both near (< 500 km) and far ranges (1000-1500 km), over a total span of almost 2000 km. Finally, panel (c) qualitatively shows that the positive perturbations (enhancements) in de-trended TEC align well with the enhancements in SuperDARN power. The relation between de-trended TEC and SuperDARN backscatter power is further investigated using a correlation analysis in Figure 6 which shows a time-series plot comparing de-trended TEC and SuperDARN power between 300-600 km and 0045 and 0200 UT (marked in Figure 5). This range-time interval is chosen because of the absence of data gaps in both datasets. In this period, peaks in SuperDARN power align well the peaks in de-trended TEC, especially between 0100 and 0130 UT. A direct correlation between the two datasts is difficult due to the differences in temporal resolutions between them and moreover, TECu is a linear unit whereas dB (SuperDARN power) is logarithmic. The 1D Pearson correlation coefficient calculated using a two minute rolling aver-

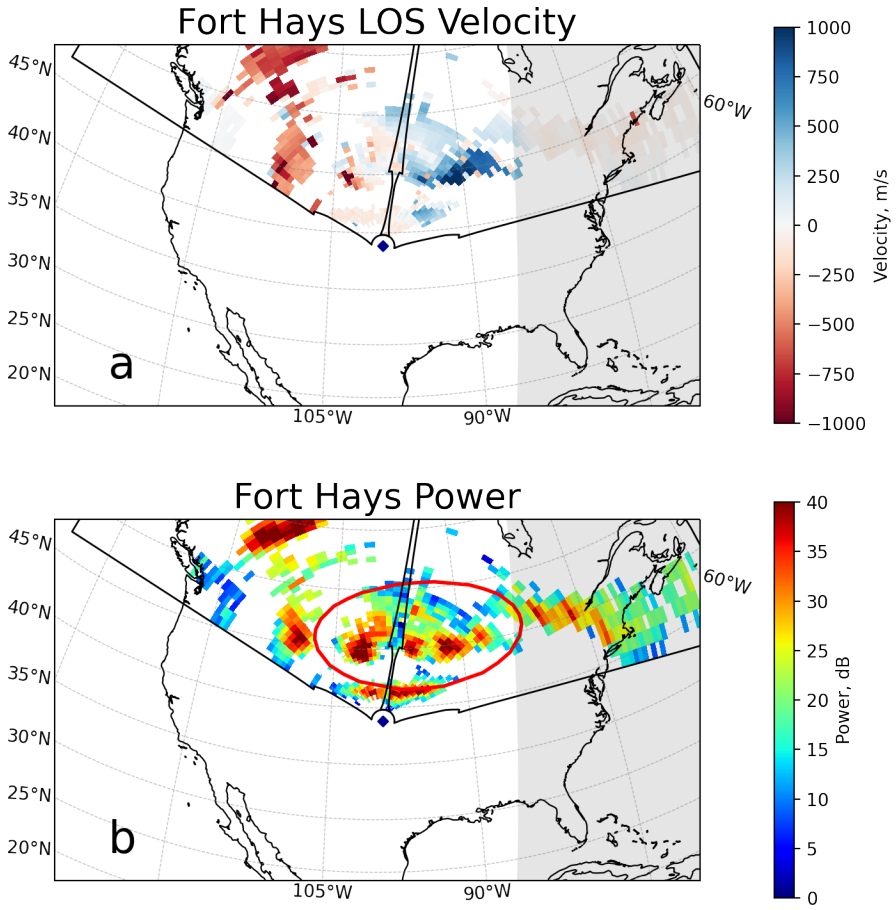

Figure 4. FHE and FHW radar measurements at 0:00UT on September 8th, 2017 (same time as Figure 2). Panel (a) presents SuperDARN LOS velocities scaled according to the color bar on the right. Panel (b) shows the SuperDARN backscatter power. The grey shaded region indicates the day-night terminator.

Table 1. MSTID Characteristics as Determined by SuperDARN and TEC

Characteristic	Value from SuperDARN (CVE 18)	Value from TEC
Wavelength	$600 - 800\ km$	$660\ km$
Phase Speed	$800 - 900\ m/s$	$800\ m/s$
Period	$10 - 20\ min$	$10 - 20\ min$

age over both the datasets was 0.29. The two datasets didn't exhibit a strong correlation, and the differences in the spatio-temporal cadence between the two datasets likely contributed to it. However, it can be qualitatively stated that the peaks in de-trended TEC aligned with enhancements in SuperDARN power. Additionally, an artifact of beam forming SuperDARN radars is that the farther beams off boresight will have non-constant azimuthal angles as elevation increases. This is known as the beam cone, and is described by (André et al., 1998). This means that it is possible that measurements by CVE beam 18 and FHE beam 18 specifically may be slightly shifted from their reported position. However, the scale sizes of the MSTIDs are larger than any potential shift due to the beam cone effect, and it will not have a significant impact on our results.

In Table 1, the characteristics of the MSTIDs estimated from both the datasets are summarized. Specifically, the wavelength, phase speed, and the time-period of the MSTIDs are presented. These values were estimated manually. MSTID period was estimated by calculating the time-interval between two phase fronts, while the phase speed was estimated by calculating the slope of the striations. The process is illustrated in Figure 5.b, where phase fronts are indicated by black lines. Beams that have a more zonal look direction are more suitable for this analysis (such as CVE beam 18 shown in the figure), since they are oriented more along the MSTID propagation direction. Note that the phase speed is different from the LOS velocities measured by SuperDARN radar. Values from SuperDARN radars show wavelengths between 500 and 1000 km, phase speeds of 800-900 m/s (LOS), and a time-period of 10-20 minutes. TEC estimates of these characteristics are in agreement. Estimates vary significantly through the event interval, as differing wave structures appear at different times. TEC estimates were made using Range-Time-Intensity (RTI) TEC plots (Figure 5), and keogram plots (Figure 3). Overall, despite the differences in spatio-temporal coverage between these two datasets, the characteristics of the MSTIDs estimated from them are largely consistent.

So far, the spatio-temporal variations in de-trended TEC and SuperDARN power have been compared and it was demonstrated that enhancements in TEC were collocated with enhancements in SuperDARN power. In Figure 7, a comparison between de-trended TEC and SuperDARN LOS vectors is presented along beam 14 of the FHE radar. In a format similar to Figure 5, panel (a) presents de-trended TEC, panel (b) shows LOS velocities along FHE beam 14, and panel (c) shows both the datasets overlaid on top of each other. Similar to the observations presented in Figure 5, strong perturbations in TEC can also be observed along this beam. Note that the color bar for SuperDARN LOS velocities shown in panel (b) is centered on 150 m/s to bring out the oscillations in velocities. It can be seen that the LOS velocities between 2330 UT and 0100 UT and 300-1200 km range oscillate around the central value with strong positive upswings collocated with enhancements in TEC. The polarity changes in SuperDARN LOS velocities become more evident in Figure 8 which is in the same format as Figure 7 but for beam 18 of the FHW radar, which is the poleward looking beam near mid-western United States (see Figure 2). (TEC coverage is sparse in the region which produces the data gaps in panel (a) of Figure 8.) The main feature that stands out from the figure is the systematic polarity change in LOS velocities as the MSTIDs pass through the beam. The color bar

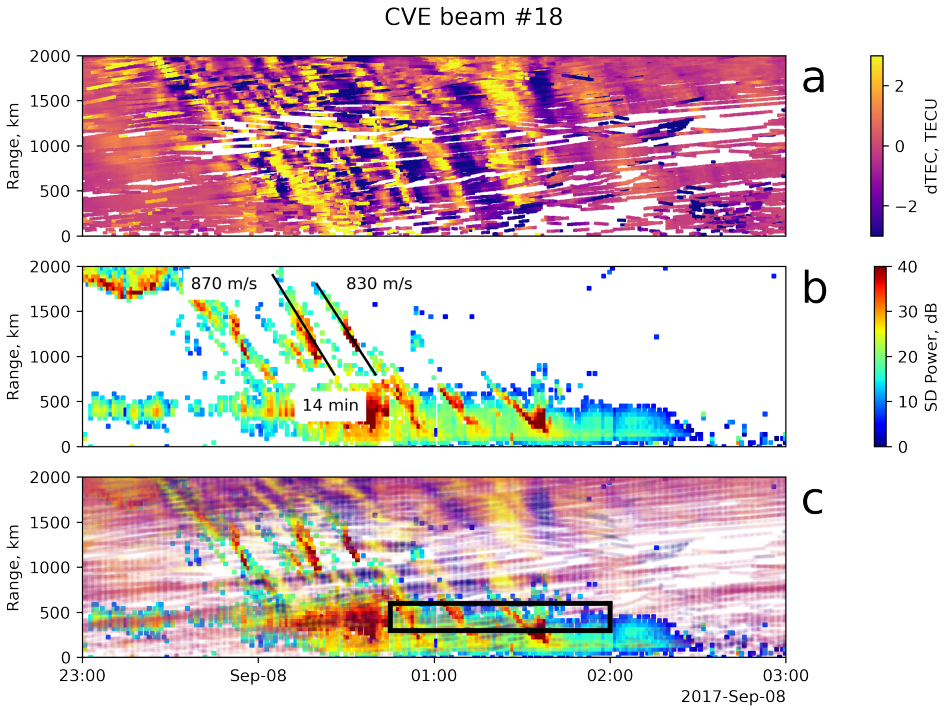

Figure 5. Comparison between SuperDARN and GNSS TEC measurements. Panel (a): de-trended GNSS TEC observations projected along CVE beam 18. Panel (b): CVE beam 18 measurements of backscatter power. Slope values allow for calculation of LOS phase speed. Panel (c) shows de-trended GNSS TEC from panel (a) and SuperDARN backscatter power from panel (b) overlaid on top of each other. The black boxed region contains data compared in 6.

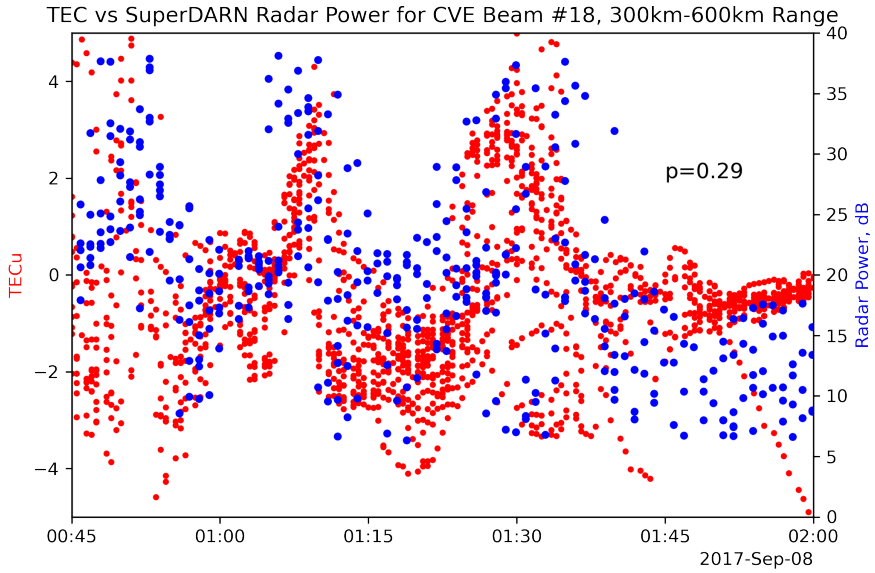

Figure 6. Time series plot showing correlation between maximum SuperDARN power level and mean detrended TEC. Data is taken between 300 and 600km along CVE Beam 18 shown in panel (c) of Figure 5. Rolling averages of the datasets are compared using a 1D Pearson correlation coefficient, resulting in p=0.29.

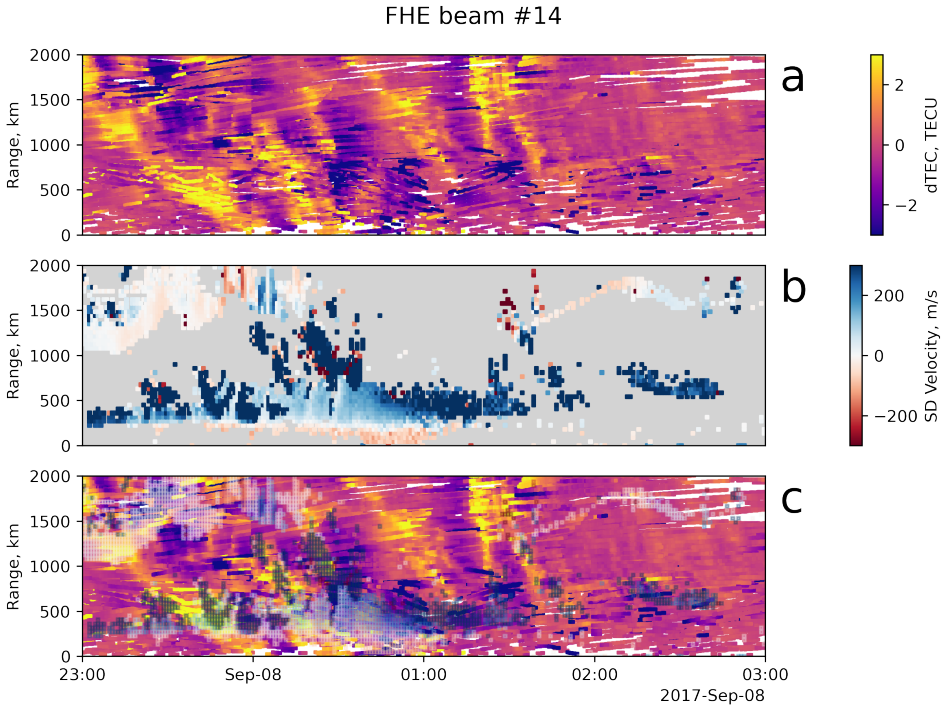

Figure 7. Comparison between SuperDARN LOS velocities and GNSS TEC measurements. Panel (a): de-trended GNSS TEC observations projected along FHE beam 14. Panel (b): FHE beam 14 measurements of LOS velocities. Panel (c) shows de-trended GNSS TEC from panel (a) and SuperDARN LOS velocities from panel (b) overlaid on top of each other.

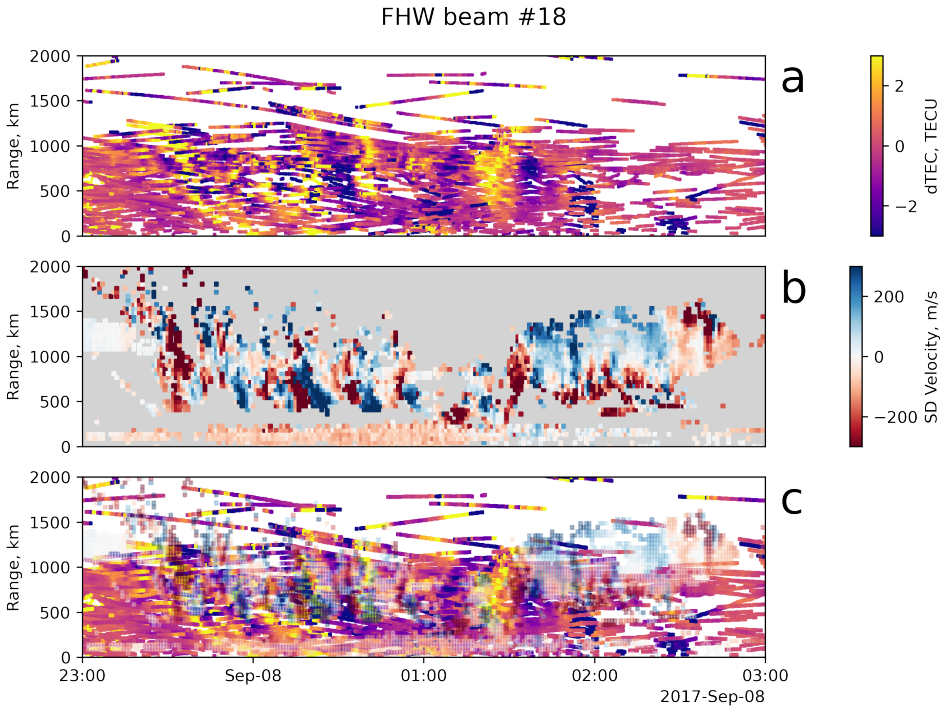

Figure 8. Same format as Figure 7 but for Fort Hays West Beam 18.

is now centered at 0, and velocities now oscillate with peak amplitudes exceeding ±300 m/s.

4 Discussion

In the previous sections, the characteristics of storm-time MSTIDs observed in high-resolution GNSS TEC and SuperDARN datasets were examined. Here, the current observations will be compared with those presented in previous studies, and the role of different factors in driving these storm-time MSTIDs will be determined.

An important feature from Figure 5 is that MSTID signatures in SuperDARN were observed in the near ranges (<500 km) as well as the farther ranges (∼1000-1500 km). Due to the nature of HF propagation, widley distributed backscatter from farther ranges is primarily due to F region irregularities, while backscatter from closer than about 600 km must be due to E region irregularities (Chisham et al., 2008). The transition in backscatter mode can be appreciated in Figure 5 with the change in backscatter characteristics that occurs at about 600 km. Here the intermittent backscatter at further ranges gives way to continuous backscatter over the E region ranges. While SuperDARN slant range can provide some additional context regarding the region of the ionosphere producing the backscatter, it is difficult to resolve altitude profiles of electron density using the GNSS TEC dataset. However, it is likely that a significant contribution to the variability observed in TEC is coming from the F region, where electron densities are expected to be the highest, even during geomagnetic storms (Hocke et al., 2019). A comparison between Figures 2 and 5 shows that the variability in TEC (indicated by dTEC) was very strong (∼50% of the background values), suggesting that the F-region electron densities might be making significant contributions to the variability observed during this event. Overall, these observations from SuperDARN and GNSS TEC suggest that there was a strong coupling between the E and the F regions of the ionosphere during this event such that

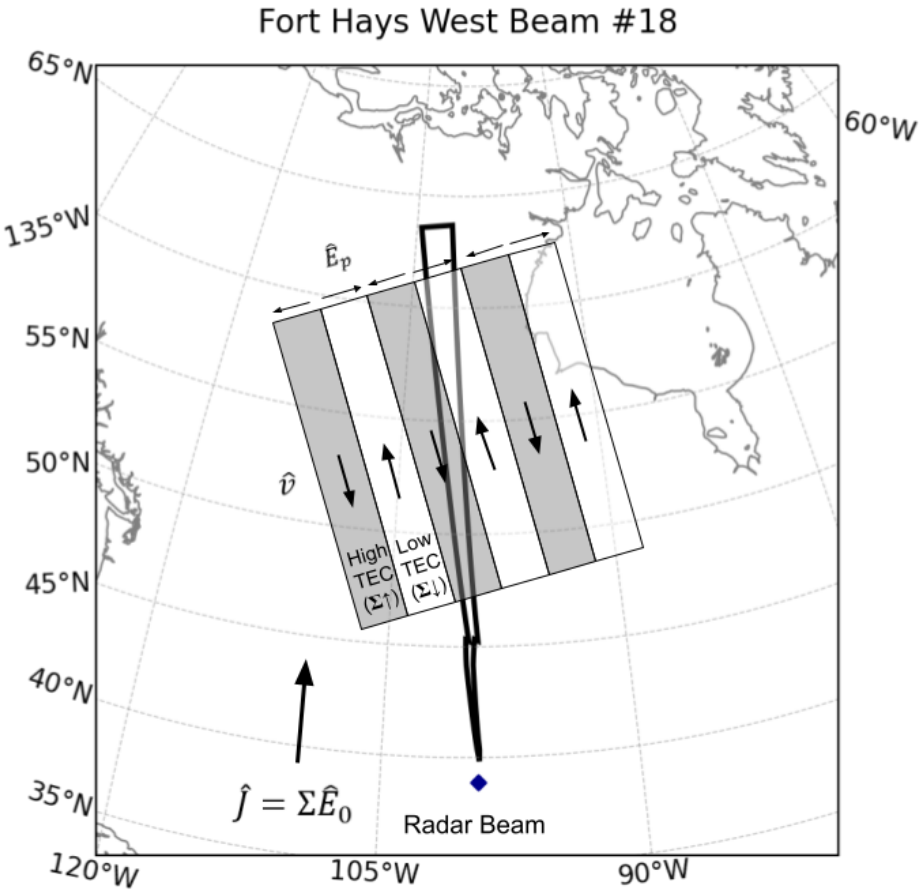

Figure 9. A schematic illustrating the proposed mechanism to explain the generation of polarization electric fields and their relation to MSTID wavefronts and background plasma convection. Polarization electric fields (E_P) are shown, as well as the resulting ExB drifts ($\hat{v}$).

MSTID signatures are observed in both regions. This raises a key question: Do these MSTIDs originate in the E-region or the F-region? It is possible that Hall current driven processes generate polarization electric fields in the E-region which map into the F region and drive MSTIDs (Tsunoda & Cosgrove, 2001). It is also possible that E region echoes in SuperDARN are modulated by MSTIDs originating in the F-region. Previous studies have suggested that coupling between the E- and the F-regions and sporadic-E layers can augment and enhance the instabilities associated with MSTIDs (Otsuka et al., 2007; Ogawa et al., 2009). The Gradient Drift Instability (GDI) was suggested to be the primary plasma instability mechanism generating field-aligned irregularities observed by SuperDARN in such a case (Hiyadutuje et al., 2022). Regardless of the source region, it is clear that inter-region electrodynamics across altitude likely play a key role in furthering the plasma instability driving these storm time MSTIDs.

From Figure 1, it can be noted that the MSTIDs reported during this event were observed during the initial phases of a major geomagnetic storm. S. R. Zhang et al. (2019) analyzed the same event using the high-resolution GNSS TEC dataset and suggested two possibilities. The first is that ion-neutral frictional heating from the westward SAPS flows in the region produces AGWs and associated MSTIDs. Global Ionosphere-Thermosphere model (GITM) simualtions presented by Guo et al. (2018) showed that strong SAPS flows can significantly heat the thermosphere and drive TIDs. The second possibility is that polarization electric fields induced by an electrodynamic instability (e.g., Perkins, 1973) are driving the MSTIDs. It is not possible to determine if electrodynamic instabilities are driving the MSTIDs based soley on GNSS TEC data. Instead, additional measurements, such as those showing polarization electric fields, are needed. A few previous studies have shown that polarization electric fields, which systematically switch polarities between the crests and troughs in MSTIDs, manifest as oscillations in SuperDARN Doppler velocities (e.g., Ogawa et al., 2009; Suzuki et al., 2009). Such oscillations in the line-of-sight Doppler velocities are clearly evident during the current event, in beam 14 of the FHE (Figure 7) and beam 18 of the FHW (Figure 8) radars. The SuperDARN observations therefore confirm the presence of polarization electric fields during this event, and are in agreement with the conjecture made by S. R. Zhang et al. (2019) that these MSTIDs are driven by an electrodynamic instability. Finally, the south-westward propagation of MSTIDs observed during this event is similar to observations of electrified MSTIDs reported previously by Ogawa et al. (2009), which has been attributed to preferential Joule damping associated with electrodynamic instability processes (Kelley, 2011).

Previous studies have used mid-latitude SuperDARN observations in the Japanese sector to identify and analyze electrified MSTIDs driven by polarization electric fields (Ogawa et al., 2009; Suzuki et al., 2009). However, these reports focused on geomagnetically quiet intervals. Consequently, the main differentiating factor between the current observations and previous reports is the strong geomagnetic driving during this event (see Figure 1). We note from Figures 5, 7, and 8 that both the radar power and LOS velocity amplitude variations are almost an order of magnitude stronger than those reported previously. These differences are perhaps unsurprising, as this study is of an intense storm time event, and the mid-latitude electrodynamics are expected to be dominated by strong SAPS electric fields (S. R. Zhang et al., 2019). During geomagnetically quiet intervals, the mid-latitude electric fields are expected to be relatively weaker and driven by neutral winds (Suzuki et al., 2009). An examination of Figure 4 shows that the background plasma convection is predominantly westwards during the MSTIDs. The spatio-temporal relationship between SuperDARN LOS velocity and TEC enhancements/depletions observed during the current event is different when compared to previous reports of quiet-time electrified MSTIDs (Otsuka et al., 2007, 2009; Suzuki et al., 2009). Specifically, enhancements in SuperDARN power during this event are aligned with enhancements in GNSS TEC (Figures 5 and 6), in contrast to quiet-time events where strong HF echoes were correlated with depletions in airglow/TEC (Otsuka et al., 2007, 2009; Suzuki et al., 2009; Ogawa et al., 2009). An interpretation of these observations is presented in Fig-

ure 9. The figure shows MSTID wavefronts passing through a poleward-directed radar beam. Regions of high TEC (conductivity) are shaded in dark. The directions of induced polarization electric fields (E_P) and the corresponding ExB drifts ($\hat{v}$) are marked in the figure. In the F-region, at mid-latitudes, the Pedersen current can be given as $J_P = \Sigma_p(E_0 + U \times B)$, here E_0 is the background electric field, U is the neutral wind velocity, and B is the magnetic field. The westward directed plasma convection observed during the event, likely associated with SAPS, suggests that E_0 is the dominant component and is predominantly northwards. U is assumed to be much smaller compared to E_0 since the event was observed during the early phases of a storm and the role of the neutral wind (the disturbance dynamo) is expected to be significant during the recovery phase (Blanc & Richmond, 1980). Consequently, J_P is also directed northwards, in the same direction as E_0. Note that the electrodynamics during the event are significantly different from the quiet-time events (Kp = 0) reported by Suzuki et al. (2009) which assume U is the dominant component and neglect the role of E_0. To maintain current continuity, polarization electric fields are induced orthogonal to the MSTID wave fronts by J_P such that they are directed north-eastwards(south-westwards) in regions of TEC depletion(enhancement). In other words, the polarization electric field has a component in the direction of J_P in regions of reduced conductivity, and away in regions of enhanced conductivity. The scenario is illustrated in Figure 9. The ExB drift associated with these polarization electric fields would be directed towards (positive LOS velocities) the radar in regions with high TEC, and away (negative LOS velocities) in regions with low TEC. Since the ExB drifts associated with the polarization electric fields are expected to be predominantly meridional, the corresponding velocity changes will be prominent in poleward-directed beams, such as beam 18 of FHW (Figure 8). This mechanism is consistent with the sense of the observations presented in Figures 7 and 8. For example, Figure in 7.b two distinct MSTID wave fronts are observed between midnight and 1:00 UT as enhancements in TEC, and corresponding SuperDARN observations show positive (blue/towards the radar) LOS velocities collocated with these enhancements.

Overall, this study presents a new class of electrified MSTIDs that are distinct from the typical quiet-time MSTIDs reported previously (Otsuka et al., 2004, 2007; Ogawa et al., 2009, e.g.,). The oscillations in SuperDARN LOS velocities and dTEC were almost an order of magnitude stronger than those observed during quiet-times (Suzuki et al., 2009) and a new mechanism has been proposed to explain the generation of polarization electric fields during intervals of strong geomagnetic driving.

5 Conclusions

This study has analyzed observations of MSTIDs during the September 7th/8th 2017 geomagnetic storm event, over mid-latitude North America. The event interval was characterized by strong geomagnetic driving with Kp reaching 9, and SymH dropping to nearly -200 nT. Signatures of MSTIDs were observed in both GNSS TEC and ionospheric backscatter in SuperDARN, with similar time-periods (∼15 minutes), wavelength (∼700km), and phase speeds (∼600 m/s). In SuperDARN, the MSTIDs produced oscillations ranging ±500m/s in LOS velocities, and in detrended GNSS TEC strong perturbations reaching up to 50% of the background TEC value were observed. These MSTIDs were propagating in the southwestward direction, similar to previous reports of MSTIDs observed on the nightside. SuperDARN data showed that the MSTID signatures were observed in both near and farther ranges, suggesting strong coupling between the E and the F-regions. Projecting detrended GNSS TEC data along SuperDARN beams showed that enhancements in TEC were positively correlated with increases in SuperDARN SNR, contrary to previous observations which showed that these parameters were anti-correlated, at least in quiet time events. Strong oscillations in LOS velocities observed in SuperDARN indicated a systematic reversal in the polarity of the electric fields between the crests and troughs of the MSTIDs, confirming the presence of polarization electric fields during the

event. The poleward directed background electric fields associated with westward directed plasma convection observed during the event were hypothesized to generate the polarization electric fields. Overall, the storm-time MSTIDs reported in this study were driven by an electrodynamic instability and were distinct from previous reports of electrified MSTIDs which were observed during quiet geomagnetic intervals.

6 Open Research

SuperDARN data can be found at the Virginia Tech SuperDARN webpage at `https://www.frdr-dfdr.ca/repo/collection/superdarn`. SuperDARN data has been processed using the Radar Software Toolkit (Burrell et al., 2022). LOS GNSS TEC data is available at `http://www.openmadrigal.org`. Individual GNSS TEC data files used in this study can be found at `https://w3id.org/cedar?experiment_list=experiments2/2017/gps/07sep17&file_list=los_20170907.004.h5` and `https://w3id.org/cedar?experiment_list=experiments2/2017/gps/08sep17&file_list=los_20170908.004.h5`. Data processing and visualization was done using open-source software, including Matplotlib (Hunter, 2007), Pandas (Wes McKinney, 2010), IPython (Pérez & Granger, 2007), Cartopy (Met Office, 2010 - 2013), Scipy (Virtanen et al., 2020), and others (Millman & Aivazis, 2011).

Acknowledgments

The authors thank the National Science Foundation for support by grants AGS-1935110, and AGS-1952737. BSRK and JBHB acknowledge National Science Foundation for support by grants AGS-1822056, and AGS-1839509. The Christmas Valley SuperDARN radars are maintained and operated by Dartmouth College under support by NSF grant AGS-1934997. SuperDARN is a worldwide collection of radars funded by various national funding agencies of Australia, Canada, China, France, Italy, Japan, Norway, South Africa, United Kingdom, and the United States of America. SuperDARN data used in this study can be accessed from the following website: `https://www.frdr-dfdr.ca/repo/collection/superdarn`. The geomagnetic indices used in this paper can be obtained from NASA's OMNIWeb service (https://omniweb.gsfc.nasa.gov/form/dx1.html). GPS TEC data products and access through the Madrigal distributed data system are provided to the community by the Massachusetts Institute of Technology under support from US National Science Foundation grant AGS-1952737. Data for the TEC processing is provided from the following organizations: UNAVCO, Scripps Orbit and Permanent Array Center, Institut Geographique National, France, International GNSS Service, The Crustal Dynamics Data Information System (CDDIS), National Geodetic Survey, Instituto Brasileiro de Geografia e Estatística, RAMSAC CORS of Instituto Geográfico Nacional de la República Argentina, Arecibo Observatory, Low-Latitude Ionospheric Sensor Network (LISN), Topcon Positioning Systems, Inc., Canadian High Arctic Ionospheric Network, Institute of Geology and Geophysics, Chinese Academy of Sciences, China Meteorology Administration, Centro di Ricerche Sismologiche, Système d'Observation du Niveau des Eaux Littorales (SONEL), RENAG : REseau NAtional GPS permanent, GeoNet - the official source of geological hazard information for New Zealand, GNSS Reference Networks, Finnish Meteorological Institute, SWEPOS - Sweden, Hartebeesthoek Radio Astronomy Observatory, TrigNet Web Application, South Africa, Australian Space Weather Services, RETE INTEGRATA NAZIONALE GPS, Estonian Land Board, Virginia Tech Center for Space Science and Engineering Research, and Korea Astronomy and Space Science Institute.

References

André, D., Sofko, G. J., Baker, K., & MacDougall, J. (1998, 4). Superdarn interferometry: Meteor echoes and electron densities from groundscatter. *Journal of Geophysical Research: Space Physics*, *103*, 7003-7015. doi: 10.1029/97JA02923

Baker, J. B., Greenwald, R. A., Ruohoniemi, J. M., Oksavik, K., Gjerloev, J. W.,

Paxton, L. J., & Hairston, M. R. (2007, 1). Observations of ionospheric convection from the wallops superdarn radar at middle latitudes. *Journal of Geophysical Research: Space Physics*, *112*, 1303. doi: 10.1029/2006JA011982

Blanc, M., & Richmond, A. (1980). The ionospheric disturbance dynamo. *Journal of Geophysical Research: Space Physics*, *85*(A4), 1669-1686. doi: https://doi.org/10.1029/JA085iA04p01669

Borries, C., Jakowski, N., & Wilken, V. (2009). Storm induced large scale tids observed in gps derived tec. *Annales Geophysicae*, *27*, 1605-1612. doi: 10.5194/ANGEO-27-1605-2009

Bristow, W. A., Greenwald, R. A., & Samson, J. C. (1994, 1). Identification of high-latitude acoustic gravity wave sources using the goose bay hf radar. *Journal of Geophysical Research: Space Physics*, *99*, 319-331. doi: 10.1029/93JA01470

Burrell, A., Thomas, E., Schmidt, M., Bland, E., Coco, I., Ponomarenko, P., ... Walach, M.-T. (2022, April). *Superdarn/rst: Rst 4.7.* Zenodo. Retrieved from `https://doi.org/10.5281/zenodo.6473603` doi: 10.5281/zenodo.6473603

Chimonas, G., & Hines, C. O. (1970, 4). Atmospheric gravity waves launched by auroral currents. *Planetary and Space Science*, *18*, 565-582. doi: 10.1016/0032-0633(70)90132-7

Chisham, G., Lester, A. M., Milan, A. S. E., Freeman, A. M. P., Bristow, A. W. A., Grocott, A. A., ... Sato, N. (2007, 5). A decade of the super dual auroral radar network (superdarn): scientific achievements, new techniques and future directions. *Surveys in Geophysics 2007 28:1*, *28*, 33-109. doi: 10.1007/S10712-007-9017-8

Chisham, G., Yeoman, T. K., & Sofko, G. J. (2008). Mapping ionospheric backscatter measured by the superdarn hf radars – part 1: A new empirical virtual height model. *Annales Geophysicae*, *26*(4), 823–841. Retrieved from `https://angeo.copernicus.org/articles/26/823/2008/` doi: 10.5194/angeo-26-823-2008

Chou, M. Y., Lin, C. C., Yue, J., Tsai, H. F., Sun, Y. Y., Liu, J. Y., & Chen, C. H. (2017, 2). Concentric traveling ionosphere disturbances triggered by super typhoon meranti (2016). *Geophysical Research Letters*, *44*, 1219-1226. doi: 10.1002/2016GL072205

Davis, T. N., & Sugiura, M. (1966). Auroral electrojet activity index ae and its universal time variations. *Journal of Geophysical Research (1896-1977)*, *71*(3), 785-801. doi: https://doi.org/10.1029/JZ071i003p00785

Ding, F., Wan, W., Ning, B., & Wang, M. (2007, 6). Large-scale traveling ionospheric disturbances observed by gps total electron content during the magnetic storm of 29–30 october 2003. *Journal of Geophysical Research: Space Physics*, *112*, 6309. doi: 10.1029/2006JA012013

Duly, T. M., Chapagain, N. P., & Makela, J. J. (2013, 12). Climatology of nighttime medium-scale traveling ionospheric disturbances (mstids) in the central pacific and south american sectors. *Annales Geophysicae*, *31*, 2229-2237. doi: 10.5194/ANGEO-31-2229-2013

Frissell, N. A., Baker, J. B., Ruohoniemi, J. M., Gerrard, A. J., Miller, E. S., Marini, J. P., ... Bristow, W. A. (2014). Climatology of medium-scale traveling ionospheric disturbances observed by the midlatitude blackstone superdarn radar. *Journal of Geophysical Research: Space Physics*, *119*, 7679-7697. doi: 10.1002/2014JA019870

Fukao, S., Kelley, M. C., Shirakawa, T., Takami, T., Yamamoto, M., Tsuda, T., & Kato, S. (1991, 3). Turbulent upwelling of the mid-latitude ionosphere: 1. observational results by the mu radar. *Journal of Geophysical Research: Space Physics*, *96*, 3725-3746. doi: 10.1029/90JA02253

Garcia, F. J., Kelley, M. C., Makela, J. J., & Huang, C. S. (2000, 8). Airglow observations of mesoscale low-velocity traveling ionospheric disturbances at mid-

latitudes. *Journal of Geophysical Research: Space Physics*, *105*, 18407-18415. doi: 10.1029/1999JA000305

Georges, T. M. (1968, 1). Hf doppler studies of traveling ionospheric disturbances. *Journal of Atmospheric and Terrestrial Physics*, *30*, 735-746. doi: 10.1016/S0021-9169(68)80029-7

Greenwald, R. A., Baker, K. B., Dudeney, J. R., Pinnock, M., Jones, T. B., Thomas, E. C., ... Yamagishi, H. (1995, 2). Darn/superdarn. *Space Science Reviews 1995 71:1*, *71*, 761-796. doi: 10.1007/BF00751350

Grocott, A., Hosokawa, K., Ishida, T., Lester, M., Milan, S. E., Freeman, M. P., ... Yukimatu, A. S. (2013, 9). Characteristics of medium-scale traveling ionospheric disturbances observed near the antarctic peninsula by hf radar. *Journal of Geophysical Research: Space Physics*, *118*, 5830-5841. doi: 10.1002/JGRA.50515

Guo, J., Deng, Y., Zhang, D., Lu, Y., Sheng, C., & Zhang, S. (2018, 3). The effect of subauroral polarization streams on ionosphere and thermosphere during the 2015 st. patrick's day storm: Global ionosphere-thermosphere model simulations. *Journal of Geophysical Research: Space Physics*, *123*, 2241-2256. doi: 10.1002/2017JA024781

Hines, C. O. (1960, 11). Internal atmospheric gravity waves at ionospheric heights. *Canadian Journal of Physics*, *38*, 1441-1481. doi: 10.1139/P60-150

Hiyadutuje, A., Kosch, M. J., & Stephenson, J. A. E. (2022, 5). First observations of e-region near range echoes partially modulated by f-region traveling ionospheric disturbances observed by the same superdarn hf radar. *Journal of Geophysical Research: Space Physics*, *127*, e2021JA030157. doi: 10.1029/2021JA030157

Hocke, K., Liu, H., Pedatella, N., & Ma, G. (2019, 4). Global sounding of f region irregularities by cosmic during a geomagnetic storm. *Annales Geophysicae*, *37*, 235-242. doi: 10.5194/ANGEO-37-235-2019

Hocke, K., & Schlegel, K. (1996, 9). A review of atmospheric gravity waves and travelling ionospheric disturbances: 1982-1995. *Annales Geophysicae*, *14*, 917-940. doi: 10.1007/S00585-996-0917-6

Huang, F., Dou, X., Lei, J., Lin, J., Ding, F., & Zhong, J. (2016, 9). Statistical analysis of nighttime medium-scale traveling ionospheric disturbances using airglow images and gps observations over central china. *Journal of Geophysical Research: Space Physics*, *121*, 8887-8899. doi: 10.1002/2016JA022760

Hunsucker, R. D. (1982, 5). Atmospheric gravity waves generated in the high-latitude ionosphere: A review. *Reviews of Geophysics*, *20*, 293-315. doi: 10.1029/RG020I002P00293

Hunter, J. D. (2007). Matplotlib: A 2d graphics environment. *Computing In Science & Engineering*, *9*(3), 90–95. doi: 10.1109/MCSE.2007.55

Iyemori, T. (1990). Storm-time magnetospheric currents inferred from mid-latitude geomagnetic field variations. *Journal of geomagnetism and geoelectricity*, *42*, 1249-1265. doi: 10.5636/jgg.42.1249

Kelley, M. C. (2011). On the origin of mesoscale tids at midlatitudes. *Annales Geophysicae*, *29*, 361-366. doi: 10.5194/ANGEO-29-361-2011

King, J. H., & Papitashvili, N. E. (2005, 2). Solar wind spatial scales in and comparisons of hourly wind and ace plasma and magnetic field data. *Journal of Geophysical Research*, *110*, A02104. doi: 10.1029/2004JA010649

Kunduri, B. S. R., Baker, J. B. H., Ruohoniemi, J. M., Nishitani, N., Oksavik, K., Erickson, P. J., ... Miller, E. S. (2018). A new empirical model of the subauroral polarization stream. *Journal of Geophysical Research: Space Physics*, *123*(9), 7342-7357. doi: https://doi.org/10.1029/2018JA025690

Liu, J.-Y., Chen, C.-H., Lin, C.-H., Tsai, H.-F., Chen, C.-H., Kamogawa, M., ... Kamogawa, M. (2011, 6). Ionospheric disturbances triggered by the 11 march 2011 m9.0 tohoku earthquake. *Journal of Geophysical Research: Space Physics*, *116*, 6319. doi: 10.1029/2011JA016761

Lyons, L. R., Nishimura, Y., Zhang, S. R., Coster, A. J., Bhatt, A., Kendall, E., & Deng, Y. (2019, 1). Identification of auroral zone activity driving large-scale traveling ionospheric disturbances. *Journal of Geophysical Research: Space Physics*, *124*, 700-714. doi: 10.1029/2018JA025980

Met Office. (2010 - 2013). Cartopy: a cartographic python library with matplotlib support [Computer software manual]. Exeter, Devon. Retrieved from `https://scitools.org.uk/cartopy`

Miller, C. A. (1997, 6). Electrodynamics of midlatitude spread f 2. a new theory of gravity wave electric fields. *Journal of Geophysical Research: Space Physics*, *102*, 11533-11538. doi: 10.1029/96JA03840

Millman, K. J., & Aivazis, M. (2011, March-April). Python for scientists and engineers. *Computing in Science & Engineering*, *13*(2), 9–12. doi: 10.1109/MCSE.2011.36

Munro, G. H. (1948). Short-period changes in the f region of the ionosphere. *Nature 1948 162:4127*, *162*, 886-887. doi: 10.1038/162886a0

Nishitani, N., Ruohoniemi, J. M., Lester, M., Baker, J. B. H., Koustov, A. V., Shepherd, S. G., ... Kikuchi, T. (2019, 3). Review of the accomplishments of mid-latitude super dual auroral radar network (superdarn) hf radars. *Progress in Earth and Planetary Science 2019 6:1*, *6*, 1-57. doi: 10.1186/S40645-019-0270-5

Ogawa, T., Nishitani, N., Otsuka, Y., Shiokawa, K., Tsugawa, T., & Hosokawa, K. (2009, 3). Medium-scale traveling ionospheric disturbances observed with the superdarn hokkaido radar, all-sky imager, and gps network and their relation to concurrent sporadic e irregularities. *Journal of Geophysical Research: Space Physics*, *114*, 3316. doi: 10.1029/2008JA013893

Otsuka, Y., Onoma, F., Shiokawa, K., Ogawa, T., Yamamoto, M., & Fukao, S. (2007, 6). Simultaneous observations of nighttime medium-scale traveling ionospheric disturbances and e region field-aligned irregularities at mid-latitude. *Journal of Geophysical Research: Space Physics*, *112*, 6317. doi: 10.1029/2005JA011548

Otsuka, Y., Shiokawa, K., Ogawa, T., & Wilkinson, P. (2004, 8). Geomagnetic conjugate observations of medium-scale traveling ionospheric disturbances at mid-latitude using all-sky airglow imagers. *Geophysical Research Letters*, *31*. doi: 10.1029/2004GL020262

Otsuka, Y., Shiokawa, K., Ogawa, T., Yokoyama, T., & Yamamoto, M. (2009, 5). Spatial relationship of nighttime medium-scale traveling ionospheric disturbances and f region field-aligned irregularities observed with two spaced all-sky airglow imagers and the middle and upper atmosphere radar. *Journal of Geophysical Research: Space Physics*, *114*. doi: 10.1029/2008JA013902

Pérez, F., & Granger, B. E. (2007, May). IPython: a system for interactive scientific computing. *Computing in Science and Engineering*, *9*(3), 21–29. Retrieved from `http://ipython.org` doi: 10.1109/MCSE.2007.53

Perkins, F. (1973, 1). Spread f and ionospheric currents. *Journal of Geophysical Research*, *78*, 218-226. doi: 10.1029/JA078I001P00218

Rideout, W., & Coster, A. (2006, 7). Automated gps processing for global total electron content data. *GPS Solutions*, *10*, 219-228.

Ruohoniemi, J. M., Greenwald, R. A., Baker, K. B., Villain, J. P., & McCready, M. A. (1987, 5). Drift motions of small-scale irregularities in the high-latitude f region: An experimental comparison with plasma drift motions. *Journal of Geophysical Research: Space Physics*, *92*, 4553-4564. doi: 10.1029/JA092IA05P04553

Saito, A., Fukao, S., & Miyazaki, S. (1998, 8). High resolution mapping of tec perturbations with the gsi gps network over japan. *Geophysical Research Letters*, *25*, 3079-3082. doi: 10.1029/98GL52361

Samson, J. C., Greenwald, R. A., Ruohoniemi, J. M., Frey, A., & Baker, K. B.

(1990, 6). Goose bay radar observations of earth-reflected, atmospheric gravity waves in the high-latitude ionosphere. *Journal of Geophysical Research: Space Physics*, *95*, 7693-7709. doi: 10.1029/JA095IA06P07693

Shiokawa, K., Otsuka, Y., Ihara, C., Ogawa, T., & Rich, F. J. (2003, 4). Ground and satellite observations of nighttime medium-scale traveling ionospheric disturbance at midlatitude. *Journal of Geophysical Research: Space Physics*, *108*. doi: 10.1029/2002JA009639

Suzuki, S., Hosokawa, K., Otsuka, Y., Shiokawa, K., Ogawa, T., Nishitani, N., ... Shevtsov, B. M. (2009, 7). Coordinated observations of nighttime medium-scale traveling ionospheric disturbances in 630-nm airglow and hf radar echoes at midlatitudes. *Journal of Geophysical Research: Space Physics*, *114*, 7312. doi: 10.1029/2008JA013963

Tsugawa, T., Otsuka, Y., Coster, A. J., & Saito, A. (2007, 11). Medium-scale traveling ionospheric disturbances detected with dense and wide tec maps over north america. *Geophysical Research Letters*, *34*, 22101. doi: 10.1029/2007GL031663

Tsunoda, R. T., & Cosgrove, R. B. (2001, 11). Coupled electrodynamics in the nighttime midlatitude ionosphere. *Geophysical Research Letters*, *28*, 4171-4174. doi: 10.1029/2001GL013245

Vadas, S. L. (2007, 6). Horizontal and vertical propagation and dissipation of gravity waves in the thermosphere from lower atmospheric and thermospheric sources. *Journal of Geophysical Research: Space Physics*, *112*, n/a-n/a. doi: 10.1029/2006JA011845

Valladares, C. E., & Sheehan, R. (2016, 9). Observations of conjugate mstids using networks of gps receivers in the american sector. *Radio Science*, *51*, 1470-1488. doi: 10.1002/2016RS005967

Vierinen, J., Coster, A. J., Rideout, W. C., Erickson, P. J., & Norberg, J. (2016, 3). Statistical framework for estimating gnss bias. *Atmospheric Measurement Techniques*, *9*, 1303-1312. doi: 10.5194/AMT-9-1303-2016

Virtanen, P., Gommers, R., Oliphant, T. E., Haberland, M., Reddy, T., Cournapeau, D., ... SciPy 1.0 Contributors (2020). SciPy 1.0: Fundamental Algorithms for Scientific Computing in Python. *Nature Methods*, *17*, 261–272. doi: 10.1038/s41592-019-0686-2

Wes McKinney. (2010). Data Structures for Statistical Computing in Python. In Stéfan van der Walt & Jarrod Millman (Eds.), *Proceedings of the 9th Python in Science Conference* (p. 56 - 61). doi: 10.25080/Majora-92bf1922-00a

Zhang, S., Erickson, P. J., Zhang, Y., Wang, W., Huang, C., Coster, A. J., ... Kerr, R. (2017, 1). Observations of ion-neutral coupling associated with strong electrodynamic disturbances during the 2015 st. patrick's day storm. *Journal of Geophysical Research: Space Physics*, *122*, 1314-1337. doi: 10.1002/2016JA023307

Zhang, S. R., Erickson, P. J., Coster, A. J., Rideout, W., Vierinen, J., Jonah, O., & Goncharenko, L. P. (2019, 12). Subauroral and polar traveling ionospheric disturbances during the 7–9 september 2017 storms. *Space Weather*, *17*, 1748-1764. doi: 10.1029/2019SW002325

Zhang, S. R., Erickson, P. J., Goncharenko, L. P., Coster, A. J., Rideout, W., & Vierinen, J. (2017, 12). Ionospheric bow waves and perturbations induced by the 21 august 2017 solar eclipse. *Geophysical Research Letters*, *44*, 12,067-12,073. doi: 10.1002/2017GL076054